A&A 659, A110 (2022)
https://doi.org/10.1051/0004-6361/202142381

Astronomy & Astrophysics

Flux rope and dynamics of the heliospheric current sheet

Study of the Parker Solar Probe and Solar Orbiter conjunction of June 2020

V. Réville[1], N. Fargette[1], A. P. Rouillard[1], B. Lavraud[2,1], M. Velli[3], A. Strugarek[4], S. Parenti[5], A. S. Brun[4], C. Shi[3], A. Kouloumvakos[1], N. Poirier[1], R. F. Pinto[4], P. Louarn[1], A. Fedorov[1], C. J. Owen[6], V. Génot[1], T. S. Horbury[7], R. Laker[7], H. O'Brien[7], V. Angelini[7], E. Fauchon-Jones[7], and J. C. Kasper[8]

[1] IRAP, Université Toulouse III – Paul Sabatier, CNRS, CNES, Toulouse, France
e-mail: victor.reville@irap.omp.eu
[2] Laboratoire d'astrophysique de Bordeaux, Univ. Bordeaux, CNRS, Pessac, France
[3] UCLA Earth, Planetary and Space Sciences, Los Angeles, CA, USA
[4] Département d'Astrophysique/AIM, CEA/IRFU, CNRS/INSU, Univ. Paris-Saclay & Univ. de Paris, 91191 Gif-sur-Yvette, France
[5] Université Paris-Saclay, CNRS, Institut d'Astrophysique Spatiale, 91405 Orsay, France
[6] Mullard Space Science Laboratory, University College London, Holmbury St. Mary, Dorking, Surrey RH5 6NT, UK
[7] Imperial College London, South Kensington Campus, London SW7 2AZ, UK
[8] BWX Technologies, Inc, Washington, D.C. 20001, USA

Received 6 October 2021 / Accepted 13 December 2021

ABSTRACT

Context. Solar Orbiter and Parker Solar Probe jointly observed the solar wind for the first time in June 2020, capturing data from very different solar wind streams: calm, Alfvénic wind and also highly dynamic large-scale structures.
Context. Our aim is to understand the origin and characteristics of the highly dynamic solar wind observed by the two probes, particularly in the vicinity of the heliospheric current sheet (HCS).
Methods. We analyzed the plasma data obtained by Parker Solar Probe and Solar Orbiter in situ during the month of June 2020. We used the Alfvén-wave turbulence magnetohydrodynamic solar wind model WindPredict-AW and we performed two 3D simulations based on ADAPT solar magnetograms for this period.
Results. We show that the dynamic regions measured by both spacecraft are pervaded by flux ropes close to the HCS. These flux ropes are also present in the simulations, forming at the tip of helmet streamers, that is, at the base of the heliospheric current sheet. The formation mechanism involves a pressure-driven instability followed by a fast tearing reconnection process. We further characterize the 3D spatial structure of helmet streamer born flux ropes, which appears in the simulations to be related to the network of quasi-separatrices.

Key words. solar wind – magnetohydrodynamics (MHD) – magnetic reconnection – methods: numerical – methods: data analysis

1. Introduction

The launch of Solar Orbiter on February 10, 2020 (Müller & Marsden 2013; Müller et al. 2020), has opened very promising opportunities for multi-spacecraft in situ observations of the inner heliosphere in conjunction with the Parker Solar Probe (PSP; Velli et al. 2020) and other spacecraft such as BepiColombo and the Solar-Terrestrial Relations Observatory (STEREO). The first measurements of Solar Orbiter were collected in the spring of 2020 over the course of a very interesting time window that coincided with PSP's fifth solar encounter. Multipoint in-situ measurements are essential in helping us understand the structure and dynamics of the inner heliosphere and, as we illustrate in this work, they are ideally complemented by 3D magnetohydrodynamic (MHD) simulations. Simpler models such as the potential source surface model (PFSS, Altschuler & Newkirk 1969; Schatten et al. 1969), while very useful overall, do not describe the plasma properties measured by the probes, in particular, the differences between steady and more dynamic solar wind states. Indeed, the degree of variability of the solar wind may be an important marker of its coronal origins (see, e.g., Antiochos et al. 2012). Here, the variability refers to fluctuations in speed, density, and magnetic field on all scales and it is different from the omnipresent turbulence that is also an important part of the more steady wind components coming from coronal holes. Turbulence in the latter states is dominated by Alfvénic fluctuations, with correlations corresponding to propagation away from the Sun, within streams of typical speeds greater than 600 km s^{-1} (see, e.g., Tu & Marsch 1995 and references therein). However, there are also slow wind streams of high Alfvénicity, as discussed in D'Amicis et al. (2021), and PSP has observed many such streams in the inner heliosphere. In contrast, what we refer to as the intrinsically dynamic solar wind component appears to be mostly slow and its fluctuations do not show strongly Alfvénic correlations. The origin of this slow wind appears to lie in proximity to closed coronal structures, such as the system of loops encountered in bipolar streamers or pseudo-streamers (Antiochos et al. 2011).

For more than twenty years, density structures propagating from the low corona into the solar wind have been observed with white-light coronagraphs and heliospheric imagers (see, e.g., Sheeley et al. 1997; Wang et al. 1998; DeForest et al. 2018).

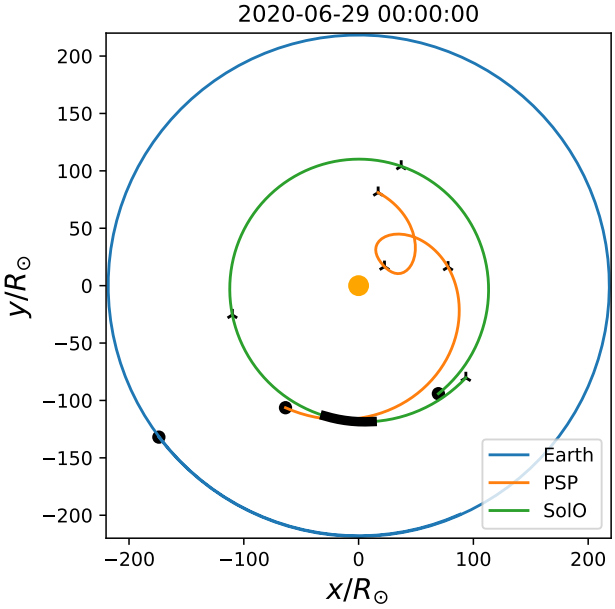

Fig. 1. Relative positions of PSP and Solar Orbiter in the solar Carrington frame on June 29, 2020. The back traced trajectory goes back to May 27 and ticks indicates the positions of the spacecraft every 11 days (the whole interval represents 33 days). The thick black line corresponds to available measurements of SWA/PAS.

These structures display some periodicity (Viall et al. 2009, 2010) and their internal magnetic structure is likely to consist of flux ropes (Sanchez-Diaz et al. 2017, 2019), namely, helical magnetic field structures that often arise from reconnection events. The HCS, although very thin, is surrounded by a thicker, denser layer: the heliospheric plasma sheet (HPS). Lavraud et al. (2020) have analyzed recent observations of PSP, arguing that the high-beta plasma of the HPS consists mainly of material expelled from a reconnection process. Numerical simulations have indeed shown that the HCS is unstable and that reconnection occurs at the tip of helmet streamers (Einaudi et al. 1999; Endeve et al. 2003, 2004; Rappazzo et al. 2005; Higginson & Lynch 2018). In Réville et al. (2020b), using high-resolution resistive 2.5D MHD simulations, we provided evidence that a fast tearing instability (Furth et al. 1963; Biskamp 1986; Loureiro et al. 2007; Pucci & Velli 2014; Tenerani et al. 2015) was the process responsible for the release of plasmoid-like structures and density perturbations.

The global picture in 3D is, however, more complex. What processes control reconnection at the base of a warped HCS? Moreover, realistic solar magnetic field can develop other substructures that can favor the accumulation of currents and reconnection. Priest & Démoulin (1995) and Démoulin et al. (1996) have developed the concept of quasi-separatrix layers (QSLs), where the connectivity of magnetic field lines, while remaining continuous, experiences large gradients nonetheless. Such QSLs can be identified computing the squashing factor, Q, which quantifies the gradients of connectivity of field lines between two arbitrary surfaces (Titov & Démoulin 1999; Titov et al. 2002; Titov 2007). These layers have been further shown to develop currents and trigger 3D reconnection (see Aulanier et al. 2005, 2006) in MHD simulations in the context of solar flares. In a different context, QSLs have been also used to explain the presence of a slow and dynamic wind at high latitudes, away from the HCS, through reconnection triggered by footpoint motions in the very low corona and propagating along the fan of pseudo-streamers (Antiochos et al. 2011; Higginson et al. 2017).

This paper is aimed at identifying and characterizing the sources of slow solar wind variability and dynamics observed close to the current sheet by PSP and Solar Orbiter. In Sect. 2, we detail the context of observations from both probes during the month of June 2020 and the procedure adopted to select the solar magnetograms used as inputs for the 3D MHD simulations. In Sect. 3, we briefly present the MHD model and compare the global outputs of two simulations with the in situ measurements of PSP and Solar Orbiter. Section 4 presents our main results. We first characterize the flux rope events in Solar Orbiter and PSP data using the magnetic field data as well in-situ measurements of ions and electrons. We note a good correspondence between the flux rope events in the data and their occurrence in the simulations and that is the basis of our study of the properties of flux ropes generated in the simulations. We show that their periodicity is consistent with the process described in Réville et al. (2020b), given the numerical constraints of 3D simulations. Finally, we discuss, for the first time, the longitudinal structure and distribution of 3D flux ropes along the HCS, and show that it could be related to the network of QSLs. We summarize and discuss these results in Sect. 5.

2. Overview of the period

2.1. Available data and spacecraft positions

During the month of June 2020, PSP went through its fifth encounter, with its perihelion at 27.8 $R_\odot$ on June 7 at 08:00 UTC. The first perihelion of Solar Orbiter occurred on June 15 at 08:00 UTC, with the closest approach at 111 $R_\odot$, about 0.5 AU. Figure 1 shows the positions of the spacecraft, in the Carrington rotating frame, on June 29, 2020, as well as each spacecraft's previous 33 days of orbital trajectory. The thick black line region shows the region where the Solar Wind Analyser Proton and Alpha Sensor (SWA/PAS, see Owen et al. 2020) was able to record measurements of the full 3D velocity distributions of ions between May 30 and June 1. Both spacecraft took measurements of the magnetic field vector during the entire encounters with the FIELDS (onboard PSP, Bale et al. 2016) and MAG (onboard Solar Orbiter, Horbury et al. 2020) instruments. In addition, PSP made plasma measurements with the SWEAP/SPC (Solar Probe Cup), SWEAP/SPAN-i (electrostatic analyzer for ions), and SWEAP/SPAN-e (electrostatic analyzer for electrons) over the whole month (Kasper et al. 2016). Its distance to the Sun varied between 27.8 $R_\odot$ and 125 $R_\odot$, while Solar Orbiter remained around 0.5 AU over the whole period. We see in Fig. 1 that Solar Orbiter has made a full rotation over the Sun in the Carrington frame and thus has taken measurements at all Carrington longitudes. As for latitudes, PSP was between -3.9 and 2.7 degrees, Solar Orbiter between 3.3 and 6.6 degrees. We note that the black region in Fig. 1 has been probed by the two spacecraft at times that are about a month apart – at the end of May by Solar Orbiter and at the end of June by PSP.

2.2. Choice of the magnetograms

In this study, for the initialization and for the magnetic boundary conditions of the MHD simulation, we used global magnetograms of the photospheric magnetic flux that were computed by the Air Force Data Assimilative Photospheric Flux Transport (ADAPT) model (Arge et al. 2010, 2013). The ADAPT maps are global magnetograms produced using data assimilation

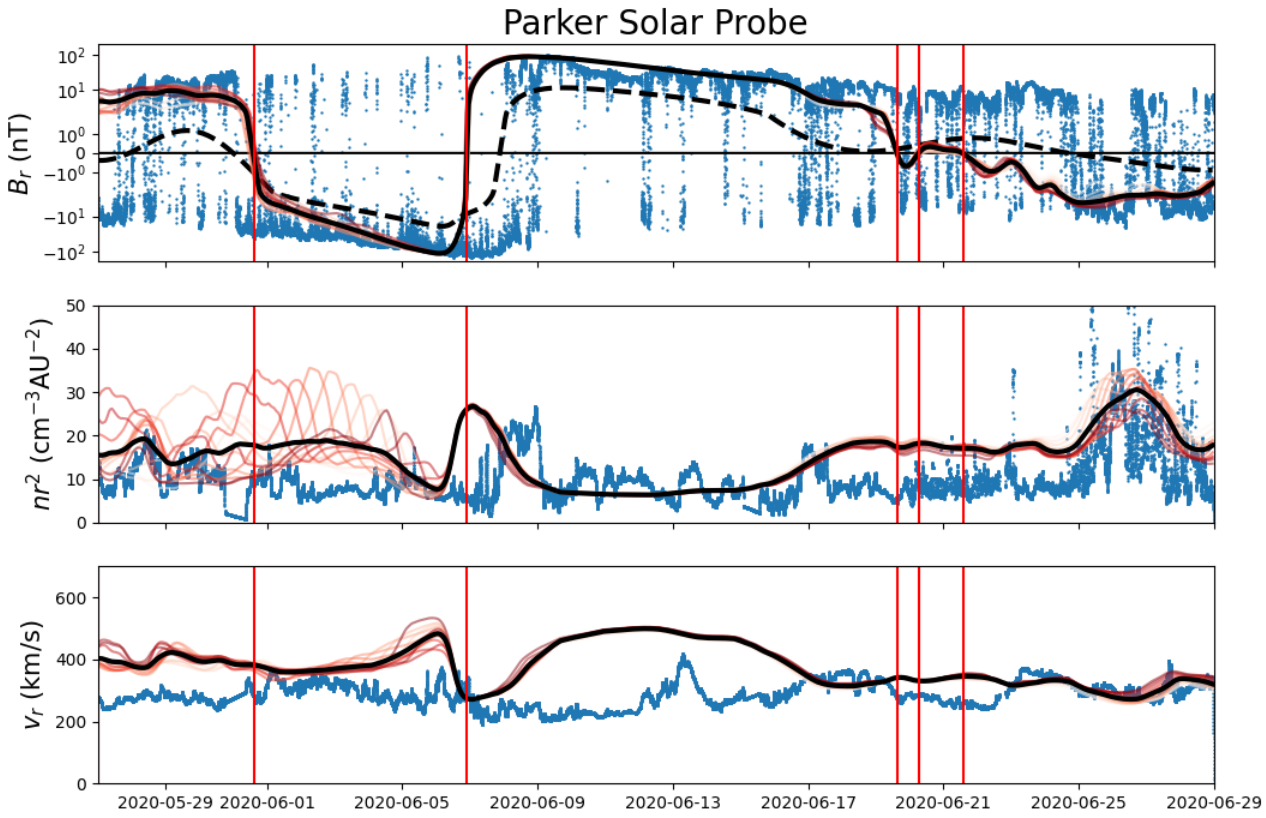

Fig. 2. In situ measurement taken by PSP between May 27 and June 29 of 2020. Magnetic field measurements are made with FIELDS, while the plasma properties are obtained with SWEAP/SPC and are shown in blue. The results of the two simulations are shown in shades of red for 13 outputs separated by two hours, while the average is shown in black. The red vertical lines are the polarity changes observed in the simulations. The PFSS solution for the radial field obtained in Sect. 2 is shown in dashed black lines in the *top panel*.

techniques based on National Solar Observatory Global Oscillations Network Group (NSO/GONG) measurements, along with a magnetic flux transport model. They provide different realizations of the photospheric magnetic field at a certain time, which are the result of the evolution of the magnetic field by the flux transport model on the far side of the Sun. In Réville et al. (2020a), we chose to rely on an ADAPT magnetogram, taken on November 6, 2018, for the whole 45-day period of the first perihelion. Some mismatch has been observed, but the overall behavior of the connection could be predicted. For this period of June 2020, connectivity studies have proved to be more difficult, possibly due to the emergence and disappearance of active regions on the solar disk (see Laker et al. 2021, for a detailed study on the shape of the HCS during this period). To prepare the MHD simulations, we thus perform a preliminary study of the sector boundaries predicted by a potential field source surface (PFSS) model (Schatten et al. 1969; Altschuler & Newkirk 1969; Badman et al. 2020). We wish to select the minimum amount of synoptic maps that best reproduce the polarity of the magnetic field measured by the two probes and, consequently, the right source for the solar wind.

We optimize the time spent within the correct polarity assuming a given magnetic map for both spacecraft, that is, we looked for the maximum of:

$$f(M) = \frac{1}{2}\int_{t_1}^{t_2} (\mathrm{sign}(B_{r,\mathrm{PSP}}(t)B_{r,M}(t)) + 1) + (\mathrm{sign}(B_{r,\mathrm{SO}}(t)B_{r,M}(t)) + 1)\,\mathrm{d}t, \quad (1)$$

where $B_{r,\mathrm{PSP}}$ and $B_{r,\mathrm{SO}}$ are the radial field measurements obtained by the two spacecraft and $B_{r,M}$ is the radial field interpolated on the projection of each trajectory on the source surface radius assuming a Parker Spiral at a given wind speed. The integrated function in Eq. (1) is equal to 1 when both spacecraft B_r measurements agree with the PFSS solution, 1/2 for only one spacecraft, and 0 otherwise. We searched for the magnetic map that maximizes $f(M)$ in all ADAPT realizations at 00:00 and 12:00 each day between May 27 and June 30 of 2020. We set as fixed parameters the source surface radius at $2\,R_\odot$, and the wind speed at $300\,\mathrm{km\,s^{-1}}$, which is close to the averaged speed observed by both spacecraft during the period (see Sect. 3.2).

We find that it is reasonable to split the month of June into two time intervals, with a given optimum for both spacecraft on each interval. We first select a period between May 27 and June 6. We find that the second realization ADAPT map of June 1 at 00:00 UTC best fits the polarity of both spacecraft before June 6. For the second period, from June 6 to June 30t, the ADAPT map of June 14 at 12:00 UTC (realization 2) gives the best score with Eq. (1). The need for a minimum of two time intervals is related to the appearance of an active region on June 3 on the solar east limb. In Figs. 2 and 3, we show, in the upper panels, the results of this preliminary study. The radial field measurements of both spacecraft are shown in blue, while the results of the PFSS models in dashed black lines.

3. MHD modeling and global results

3.1. Alfvén wave-driven MHD model

We used the Alfvén wave-driven MHD model of Réville et al. (2020a), which we call WindPredict-AW, to unravel the global

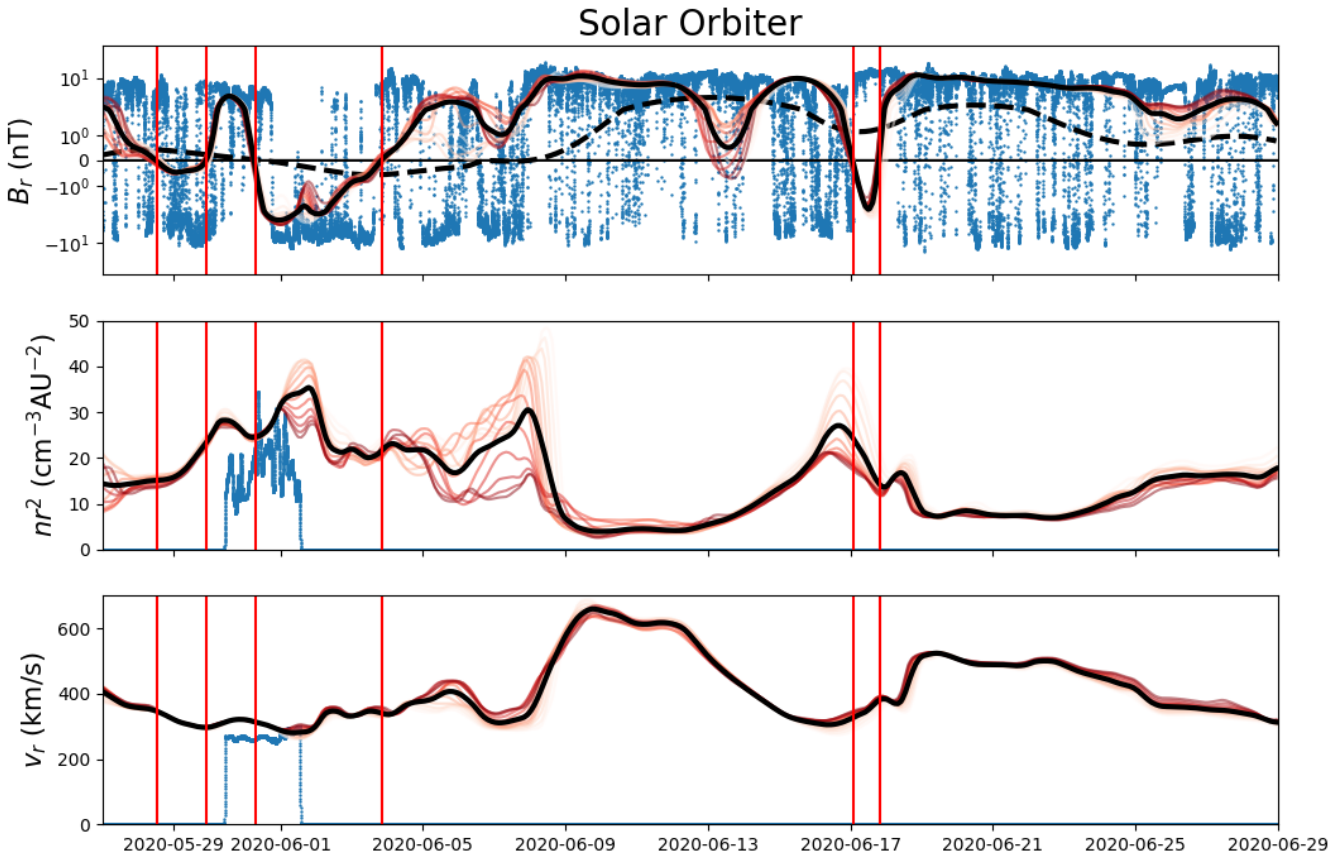

Fig. 3. In situ measurement taken by Solar Orbiter between May 27 and June 29 of 2020. Magnetic field measurements are made with MAG, while the plasma properties are obtained with SWA/PAS (only two days of measurements). The results of the plasma measurements interpolated in the simulations are shown as in Fig. 2. The PFSS solution for the radial field obtained in Sect. 2 is shown in dashed black in the *top panel*.

heliospheric structure at the time of the measurements. The full set of equations and boundary conditions can be found in the latter paper, although some further improvements have been made to the model. First, as in Réville et al. (2020b), the non-solenoidal condition on the magnetic field is ensured through the constrained transport method (Dedner et al. 2002). This feature is actually important when dealing with increasingly complex magnetic field associated with field aligned thermal conduction. The divergence cleaning method used in Réville et al. (2020a) can create oscillations in the field direction and subsequent numerical instabilities due to the behavior of the thermal conduction in small coronal loops (in regard to the resolution) typical of active regions. Hence, as the solar cycle goes to a more active phase, we found this update to be a very useful feature of the PLUTO code (Mignone et al. 2007), which WindPredict-AW is based on.

Second, the model domain now includes the transition region. The inner boundary condition lies in the chromosphere with temperature of 2×10^4 K. The density is set to a value of $2 \times 10^{10}\,\mathrm{cm}^{-3}$. We implemented the technique described in Lionello et al. (2009) to thicken the transition region in order to ease the numerical computation and limit the numerical resolution needed. The transverse velocity perturbation parameter, which controls the amplitude of the Alfvén waves launched in the domain, is set to $\delta v = 12\,\mathrm{km\,s}^{-1}$. This is lower than the value used in Réville et al. (2020a), as Alfvén waves are strongly amplified in the transition region. The input Alfvén wave pointing flux is $F_p = \rho_\odot v_A \delta v^2 \sim 1.5 \times 10^5\,\mathrm{erg\,cm}^{-2}\,\mathrm{s}^{-1}$. For this study, we use uniform grids in the angular direction, with 160 and 320 cells in the θ and ϕ direction, namely, a 1.125 degree resolution. In the radial direction, the grid is separated in three regions. The first region, meant to render the modified transition region, has 10 cells between 1.0 and 1.004 $R_\odot$. The grid is then stretched up to 15 $R_\odot$, with a minimal resolution of 0.5 $R_\odot$ and stretched again up to 130 $R_\odot$, with the largest radial grid size of 4 $R_\odot$. The simulations are performed in the rotating Carrington frame with a sidereal period of 25.38 days for a duration of 176 h (physical time) on the Jean-Zay super computer (IDRIS/CNRS France). The two simulations represent roughly 800k CPU hours.

3.2. Comparison with in situ data

We go on to compare the results of the MHD simulation with the data of PSP and Solar Orbiter. Figure 2 shows three panels with the radial magnetic field, the radial velocity, and the particle density. The magnetic field is shown in symmetrical logarithmic scale to better cope with the variation of PSP's distance to the Sun. Similarly, the density is normalized to the radial distance squared, expressed in astronomical units. The data is shown in blue. We show, at a one-minute resolution, the magnetic field measurements from FIELDS as well as the radial proton speed and density derived from the L3 moments of the SWEAP/SPC measurements. The PSP coordinates are retrieved from the open-source python package *heliopy* (Stansby et al. 2021) and converted to the Carrington frame of the simulations. Then we interpolate the simulations' fields along the spacecraft trajectories. We superpose the results of several outputs of the simulations in red shading, spaced by 2 h between $t = 132$ h and $t = 158$ h, and

show the average in black. The transition between the first and the second simulation is done over 6 h centered around June 6, 2020 12:00 UTC. The red vertical lines correspond to the heliospheric current sheet crossings detected in the simulation, corresponding to sign changes of the B_r average profile.

Looking solely at the black averaged line, one notices an overall agreement for the main large-scale fluid moments between the simulations and the data. On PSP's solar approach, from May 27 to the perihelion of June 7, we observe one main HCS crossing, which is well reproduced by the simulation using the map of June 1. The amplitude of the radial magnetic field appears fully consistent with the data, especially away from the current sheet, which is, however, less sharp in the simulation than in reality. Around the time of this HCS crossing, we observe strong perturbations in the density as well as smaller ones in the radial velocity. They are due to a very large scale flux rope propagating in the simulation. Close to PSP's perihelion, there is another HCS crossing, which occurs around June 6 22:00 UTC in the simulation, roughly one day before the data. Despite this delay, the structure of the HCS crossing in the magnetic field and in the density is well reproduced by the simulation. An episode of very calm wind then follows, up to June 18. Again, the magnetic field and the density are close to the averaged data. The model predicts, in general, a faster wind speed, especially for this quiet wind interval, where the simulation speed is around 500 km s^{-1}, against an average of 300 km s^{-1} in the data. The data still shows a velocity peak of 400 km s^{-1} around June 14.

Starting roughly after June 17, the wind comes back to a denser, slower, and variable state – as seen both in the data and in the simulation (based on the June 14 map). As we discuss in the next section, PSP measured a wind pervaded by multiple HCS crossings and small to average size flux ropes. This variability is also present in the simulation, as shown by the deviation from the average of the red curves in the density, velocity, and magnetic field. Finally, late in the month (June 27), we observe a full crossing of the HCS associated with an increased in density. The crossing is not reproduced by the simulation, but the density increase is, which means that the simulated HCS is close to PSP's coordinates at these times.

We repeat the same operation in Fig. 3 with the data of Solar Orbiter. The magnetic field is again displayed in symmetrical logarithmic scale, cadenced at one minute, and comes from the L3 public data of the MAG instrument. The density and the velocity panels display the data obtained with the proton and alpha sensor onboard Solar Orbiter. The SWA/PAS measurements represent about two days of data and include one current-sheet crossing, which is well reproduced by the simulation. Between May 27 and June 9, Solar Orbiter crossed the HCS many times and measured a lot of variability, which is consistent to the variability present in the simulations. Later on, the wind is faster and calmer, except for two briefs magnetic polarity changes simulated on June 13th and June 17, which seem to correspond to multiple HCS crossings measured in situ at these times.

4. HCS dynamics and flux ropes

4.1. Flux rope characterization in Solar Orbiter and PSP data

In this section, we further study the dynamics and variability observed in the data and the simulations. Despite the very short time window of PAS measurements, we have been able to identify in Solar Orbiter's data a series of probable flux-rope signatures on May 30 and May 31. In Fig. 4, we show the magnetic-field components in the RTN frame as well as PAS' proton density measurements. We observe characteristic features of flux ropes: increase of the total field strength, changes in plasma density and temperature, and a sign change of one of the magnetic field components. Solar Orbiter was close to the HCS at the time of these events and crossed it a few hours later (red line in Fig. 4). The marked flux rope periods show a bipolar structure in B_N, which is the normal component to the spacecraft trajectory, but is also likely to be close to the normal to the HCS. They also show a strong tangential component B_T, which is consistent with a configuration where the flux rope is mostly in the plane of the HCS.

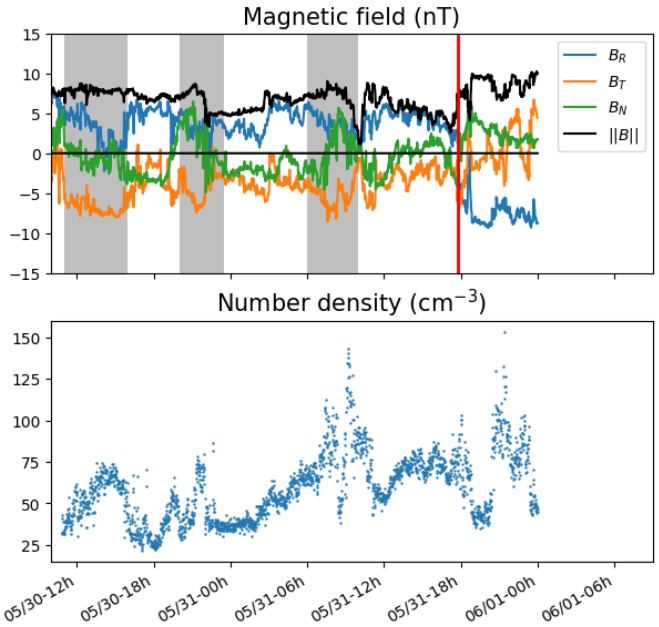

Fig. 4. Probable flux rope events (in gray) observed by Solar Orbiter on May 30 and 31 before crossing the HCS (in red). All events are characterized by an increase of the total field strength and density and a bipolar structure in one component of the magnetic field (here B_N).

As shown in Fig. 1, the same region of the inner heliosphere was probed by PSP about a month later and found to exhibit similar features. In Fig. 5, we show the structure of two flux rope events measured by PSP near June 20. To the previous analysis we add the electron pitch-angle distribution (PAD), shown in the top panel and obtained with SWEAP/SPAN-e. We focus on the eighth channel of SPAN-e, which captures electrons with energy between 283.9 and 352.9 eV, corresponding to the suprathermal strahl electron population at this distance from the Sun (see, e.g., Gosling et al. 2005). The first event is on the left of the panel (starting on June 19 at 18:00), where we observe an increase in the total magnetic field strength, as well as a full reversal of the radial and normal field. The pitch-angle distribution shows electrons fluxes aligned and anti-aligned to the magnetic field, suggesting that we are in a structure connected to the Sun at both ends. The second event occurs right after a HCS crossing and lasts from June 20 at 12:00 to June 21 at 1:00 UTC. We see a smaller increase of the magnetic field amplitude, with a reversal of B_N. The plasma density drops somewhat, while the PAD show electron fluxes parallel to the magnetic field, which means that the structure is connected to the Sun at one end only. Right after the flux rope (in gray), we also observe a strahl electron dropout that is characteristic of a reconnection region disconnected from the Sun (Gosling et al. 2005).

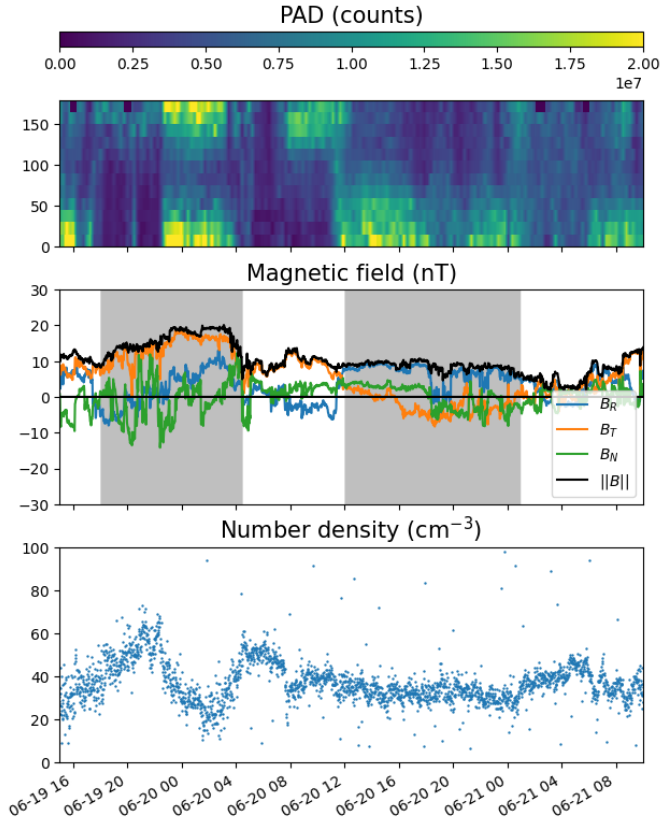

Fig. 5. Two flux ropes structure identified in PSP data. *Top panel*: PAD from SPAN-e, in arbitrary count units, of electrons between 283.9 and 352.9 eV. *Middle and bottom panels*: structure of the magnetic field in the RTN frame and the plasma density (SWEAP/SPC). The two gray shaded area indicate the position of flux ropes with different connectivity visible in the PAD, uni-directional (right) and bidirectional electrons (left).

We then go on to consider the whole month of PSP measurements. A joint analysis of the PAD, magnetic field, density, and velocity field is performed to identify HCS crossings and flux using four different instruments: FIELDS, SWEAP/SPC, SWEAP/SPAN-i, and SWEAP/SPAN-e, and summarized in Fig. 6. The first panel resembles the first panel of Fig. 2, but shows additional information. The variability of the radial field in the simulations is shown in shaded red, representing the min and the max value of the curves shown in Fig. 2. The total measured magnetic field is plotted in black, overlaid in red is the occurrence of flux rope or HCS (partial) crossings. Appendix B lists and labels all the events represented in red, with precise start and stop times. The PAD is normalized to the energy integral for a given time, as the electron counts vary greatly with heliocentric radial distance. The third panel shows the cross-helicity of the solar wind perturbations defined by:

$$H_c = \frac{2\delta\mathbf{v}\cdot\delta\mathbf{b}/\sqrt{4\pi\langle\rho\rangle}}{\delta v^2 + \delta b^2/(4\pi\langle\rho\rangle)}, \tag{2}$$

where

$$\delta\mathbf{v} = \mathbf{v} - \langle\mathbf{v}\rangle, \tag{3}$$
$$\delta\mathbf{b} = \mathbf{B} - \langle\mathbf{B}\rangle, \tag{4}$$

and where the averaging operator $\langle\rangle$ represents a running average of one hour. It is interesting to notice the good correspondence between the pitch-angle distribution and the cross-helicity defined this way. Because electrons are always streaming away from the Sun, when the interplanetary magnetic field is globally Sunward, the PAD distribution is mainly concentrated around 180 degrees. In such situation, for a relatively calm wind, Alfvén waves are expected to propagate away from the Sun too and the correlation between the velocity and magnetic field perturbations is positive, yielding a cross-helicity up to one. This correspondence works well for the beginning of the interval up to June 17. We also observe clear changes in the pitch-angle distribution of suprathermal electrons (going from 0 to 180 degrees or the opposite), which are indicators of HCS crossings, for instance, on May 29 and on June 8 right after PSP's perihelion.

The last panel of Fig. 6, shows the plasma β parameter obtained with SPC and SPAN-i: β covers a wide range of values, sometimes below one, but clear enhancements are observed either close to the HCS crossing or during flux-rope events. After June 17, the PAD shows fast variations of streaming electron directions, as well as strahl electron dropouts. The cross-helicity also suddenly rises when the polarity of the magnetic field stays globally positive. This period between June 17 and June 25 is a very good example of what happens when PSP cruises very close to the HCS. In addition to multiple crossings, many flux ropes are observed, which is interestingly very consistent with the variability seen in the simulations, as shown in Fig. 2.

4.2. Origin of simulated flux ropes

We consider the process that is possibly responsible for the creation of these flux ropes. In our simulations, after roughly 60 h of simulated time, reconnection develops in the current sheet between 5 and 10 solar radii. Following this reconnection, helical structures –flux ropes– are created and they propagate in the solar wind. In Fig. 7, we show snapshots of the June 14 simulations at two different times. In the left panel, at $t = 112.8$ h, we show a 2D cut at $\varphi = \pi$ (180° longitude) of the corona and solar wind velocity along with selected field lines around the current sheet. The middle panel displays the perturbed tangential Alfvén speed for the same time interval. The average $\langle v_{A,\theta}\rangle$ is computed over an interval of 20 h around the reconnection time. Above the main streamer, we observe a growing long wavelength mode characteristic of the tearing instability. This perturbation is propagating and (at $t = 112.8$ h) it is about to fully cross the Alfvén surface (in white). In the bottom panel, we render a 3D view of the magnetic-field geometry. We observe a tilt of the field lines to the left, which is a sign of the presence of a tangential field oriented along $-\mathbf{e}_\varphi$. Field lines in red have started the reconnection process (noting that they are not exactly corresponding to the 2D view). On the right side of Fig. 7, we show the same features, at $t = 115.1$ h. The HCS has reconnected and created a flux rope following the tangential or "core" field orientation. Magnetic footpoints of the flux rope have considerably shifted to the right and the structure extends to about 50 degrees of longitudes. We can see the markers of the acceleration following the reconnection, with field lines advected further away on the left than on the right.

In Fig. 8, various 3D quantities are extracted along the HCS at $15\,R_\odot$ for the June 14 simulation. Signatures of the reconnection process can be seen easily in the latitudinal magnetic field. Density enhancements are located on the front of the flux ropes, consistently with the picture given in Sanchez-Diaz et al. (2017, 2019). Flux ropes are more present at certain longitudes. Figure 8 shows a rather extended perturbed front between 130

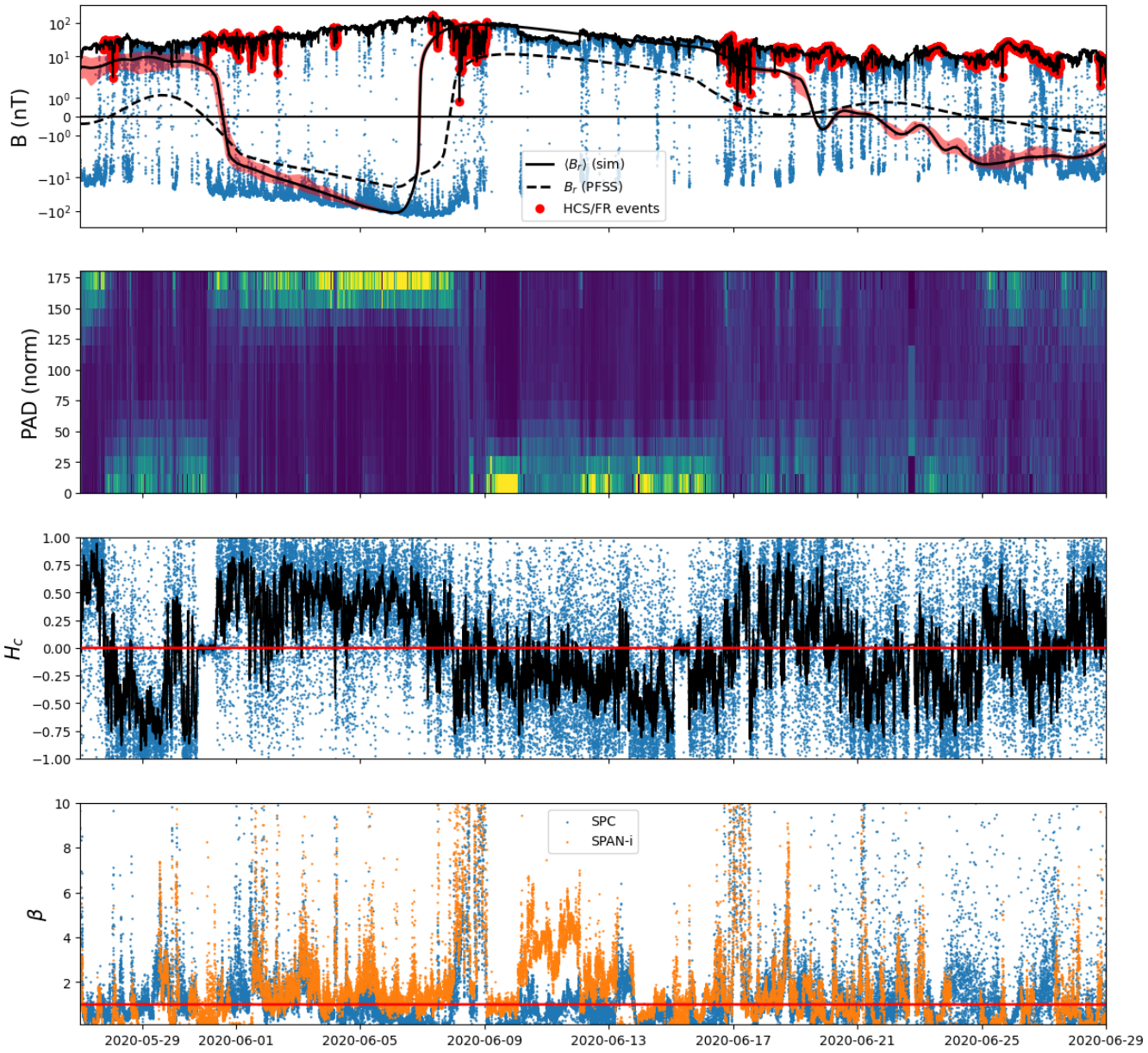

Fig. 6. PSP measurements of dynamical structures. In the *first panel*, we show the observed radial (blue) and total (black) magnetic field over the month of June. The results of the simulation and of the PFSS models are repeated from Fig. 2, and the variability of the simulations is shown in shaded red. Red points identify flux rope events and partial or total HCS crossings observed in the data on the total magnetic field line. They are further identified with the *second panel*, showing the normalized pitch-angle distribution of electrons in the eight channel of SPAN-e, around 300 eV. The *third panel* shows the cross-helicity of perturbations in the velocity and magnetic field, and is close to one in negative polarity, close to minus one in positive polarity of the interplanetary magnetic field. The *bottom panel* shows the value of the plasma beta parameter obtained with SPC and SPAN-i, and the red line indicates a value of $\beta = 1$.

and 300 degrees of longitudes. This front is likely made of several structures released periodically. Another smaller flux-rope front is observed around a longitude of 360 at the top of the figures. To characterize the periodicity of these multiple flux ropes, in the bottom panel of Fig. 8 we plot the temporal Fourier spectra of all four quantities computed for each longitude. For the main flux rope structure, there is a clear peak at a frequency of $0.05\,\mathrm{h}^{-1}$– or a periodicity of 20 h. This periodicity is also seen in the smaller structure at longitudes around 360 (it is especially visible in the spectral plot of B_θ). The process at the origin of these periodic release is thus relatively independent of the longitude and of the magnetic structure of the corona. In Réville et al. (2020b), we identified two characteristic periods. The longer periodicity (around 30h in Réville et al. 2020b), was proposed to be associated with the formation and re-formation of the tip of the helmet streamers, whose timescales are related to the coronal heating process of the simulation. We find this longer periodicity here with the 3D simulations, a periodicity that is also observed in the solar wind (e.g., Viall & Vourlidas 2015; Sanchez-Diaz et al. 2017) and noted in other works on the instability of streamers (Endeve et al. 2003; Higginson & Lynch 2018).

This period of between 10 h and 30 h can be understood as the result of a pressure-driven instability followed by the tearing of the current sheet, which leads to magnetic reconnection. Simply put, at the tip of helmet streamers, the pressure gradients are sufficient to transport plasma parcels against the magnetic

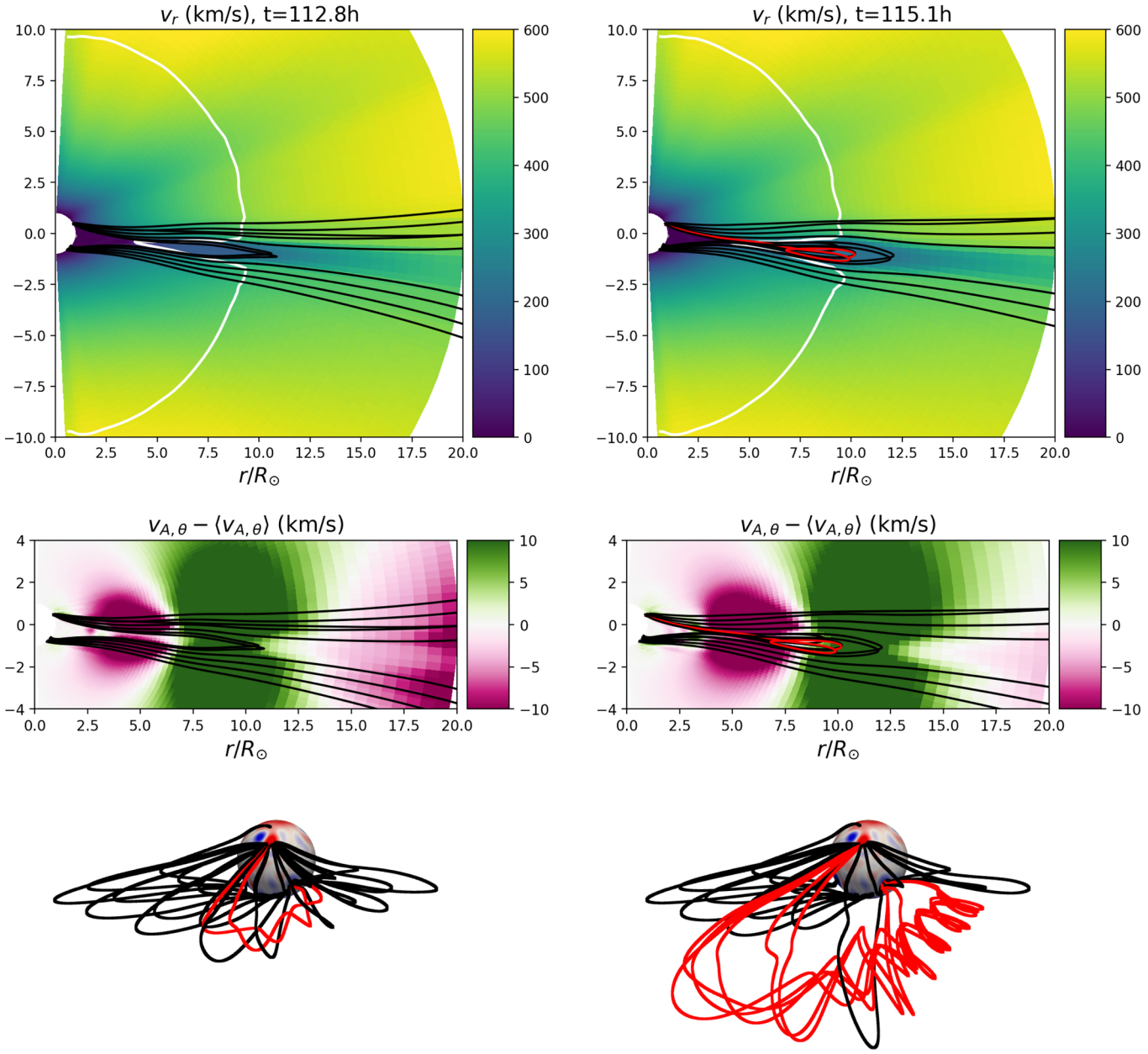

Fig. 7. Onset of the reconnection in the June 14 simulation. *Top panels*: 2D view of field lines traced from the HCS and connecting to the surface at two epochs, $t = 112.8$ h and $t = 115.1$ h. The view is a cut at $\varphi = \pi$ (180° longitude). The background color shows the velocity field. The white rounded curve shows the Alfvén surface. Field lines are plotted in red when they possess helical structures. *Middle panel*: perturbations in the tangential field (in units of Alfvén velocity). A large-scale tearing mode can be clearly identified at the reconnection locus. *Bottom panel*: 3D view of the same epoch before and after the main reconnection event and the creation of the flux rope.

tension of the closed loop. This then results in an elongation and thinning of the current sheet that becomes unstable to a tearing mode. This process has been described experimentally by Peterson et al. (2021) and we follow a modified version of the heuristics proposed in this work, to compute the typical timescale of the lengthening of the current sheet. Defining $\kappa = (\mathbf{B}\cdot\nabla)\mathbf{B}/\|B\|^2$, the magnetic field curvature vector, $p = p_{\rm th} + p_w$, the sum of the thermal and wave pressure, and $\mathbf{g}$ the acceleration of the Sun's gravity, the transverse displacement ξ for a parcel of plasma can be written (neglecting the terms in $1/\beta$, see Peterson et al. 2021):

$$\frac{1}{R_c}\frac{\partial^2\xi}{\partial t^2} = \kappa\cdot\left(\frac{c_s^2}{p}\nabla p - \mathbf{g}\right), \tag{5}$$

where $R_c = 1/\|\kappa\|$, is the curvature radius of the magnetic field. When the right-hand side of Eq. (5) is negative, the magnetic tension can confine the plasma inside the helmet streamer. When it is positive, the plasma displaced according to the solution of Eq. (5):

$$\xi(t) = R_c\left[\kappa\cdot(c_s^2\nabla p/p - \mathbf{g})\right]t^2/2. \tag{6}$$

Typically, as shown in Fig. 7, the plasma parcel is displaced out to $10\,R_\odot$, while the tip of helmet streamers is located around $2\,R_\odot$, hence $\xi \sim 8\,R_\odot$. The periodicity of the whole process can thus be computed as:

$$P_{\rm cr} = \mathrm{sign}\left[\kappa\cdot(c_s^2\nabla p/p - \mathbf{g})\right]\sqrt{\frac{2\xi}{|R_c\kappa\cdot(c_s^2\nabla p/p - \mathbf{g})|}}, \tag{7}$$

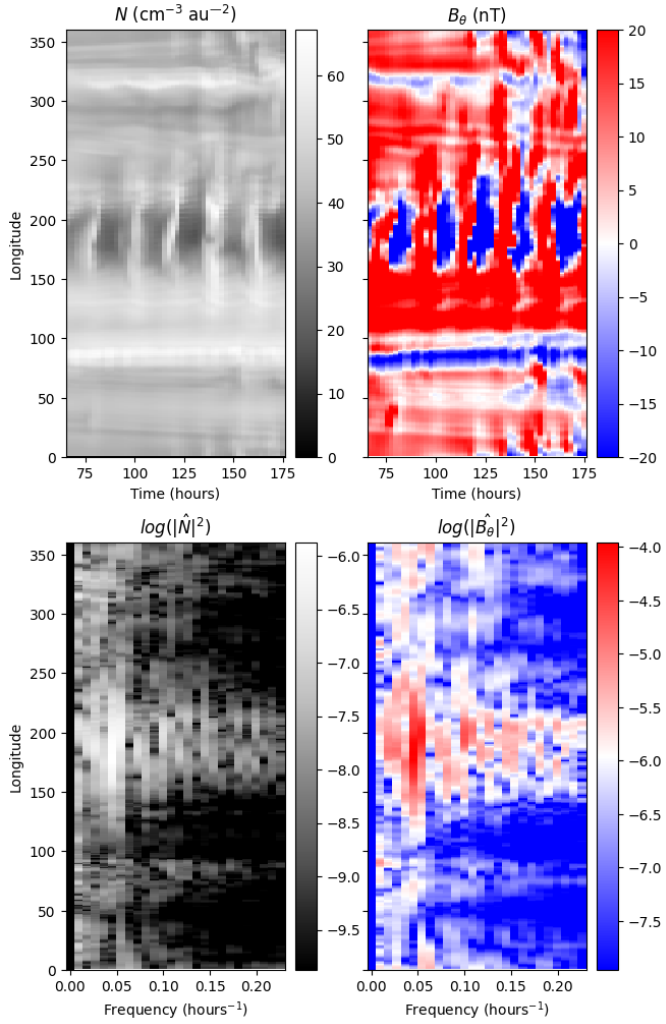

Fig. 8. Variability of the HCS at 15 $R_\odot$ for the June 14 simulation. In the *top panel*, the number density, N, and the latitudinal magnetic field, B_θ, are extracted along the HCS and stacked over time. Several propagating flux ropes are going through the domain, with various longitudinal extents, but a rather steady time pattern. In the *bottom panel*, we show a Fourier analysis over time (for each longitude). For all quantities, the peak is located around a period of 20 h.

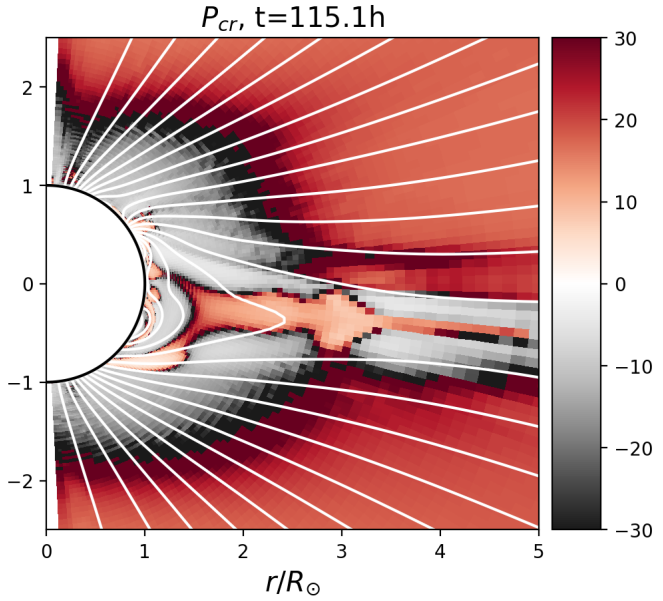

Fig. 9. Period of the pressure driven instability in the close corona. The panel shows a meridional cut at $\phi = \pi$ (180° longitude) for the June 14 simulation. Grey regions mark stable zones. In the inner corona, we clearly identify the tip of helmet streamers and the HCS as unstable zones, with a typical value of $P_{\rm cr} \sim 10{-}30$ h.

where we kept the sign function to characterize stable regions ($P_{\rm cr} < 0$). Figure 9 shows a 2D colormap of $P_{\rm cr}$. Computing the average period inside unstable regions of a shell between $r = 1.3\,R_\odot$ and $r = 2\,R_\odot$, we get $\langle P_{\rm cr}\rangle \sim 19$ h, which is very close to the typical period obtained in the simulations. We note that the boundaries between stable and unstable zone might play a significant role in this average value, which makes sense as these boundaries will be the first displaced during the process.

This process shares many similarities with our previous work in 2.5D. In Réville et al. (2020b), we proposed that the main process responsible for reconnection at the current sheet is a tearing mode. The time to thin the current sheet and trigger reconnection was between 60 h and 90 h and increasing with $S = Lv_A/\eta$, the Lundquist number. A tearing mode was then created, with plasmoids ejected beyond the Alfvén critical point in the slow solar wind. The typical scale of the plasmoids is a decreasing function of the Lundquist number, and we found, for low S regime, a wavelength of about $2\,R_\odot$, which is roughly what we observe here in 3D. In the 2.5D study, the Lundquist number had to be higher than a critical value of $\sim 10^4$ for the tearing mode to be triggered. In the present 3D simulations, we do not include explicit resistivity and as such, it is the numerical resistivity that acts for the reconnection process. Because of computational costs, it is much harder to reach the necessary resolution for a proper description of the tearing process. Using a simple dimensional analysis, we can estimate $\eta = V\Delta L$, where V is a typical wave speed of the problem, say the Alfvén speed and ΔL the grid resolution. The numerical Lundquist number $S = Lv_A/\eta$ then reduces to $S_{\rm num} = L/\Delta L$, and considering the reconnection region ($r = 5\,R_\odot$) and the resolution across the current sheet we get $S_{\rm num} \sim 500{-}1000$, which is below the threshold observed in 2.5D resistive MHD. However, it is also possible that in 3D the onset of the tearing mode is lowered due to the presence of the core field or complex magnetic fields coming from the magnetic map. One important effect is an "effective" finite extent of the x-line in the third dimension that might allow a disconnection of a flux rope even at low S. Nevertheless, the high value of S revealing asymptotic behavior characterized by an extremely thin sheet with the formation of plasmoid chains and secondary tearing (seen in Réville et al. 2020b) is absent in the 3D simulation and further research is necessary to better characterize this process in 3D.

Such 3D simulations can provide valuable information on the distribution and the longitudinal and latitudinal extent of these flux ropes. 2.5D plasmoids should generalize to full torii in 3D, but this is obviously not what we observe here in our simulations (see Fig. 7) and more generally in the solar wind (Rouillard et al. 2008, 2010). Simulated flux ropes are confined in latitude, extending by a few degrees above and below the HCS. In the simulations, flux ropes show different kinds of connectivity. As shown in Fig. 7, they start connected to the solar surface by both legs, which would correspond to observed bidirectional electrons in Fig. 5. But we have also observed configurations where the flux rope is connected on one end to the Sun and the other one into the solar wind, corresponding to the uni-directional electron flux shown in Fig. 5.

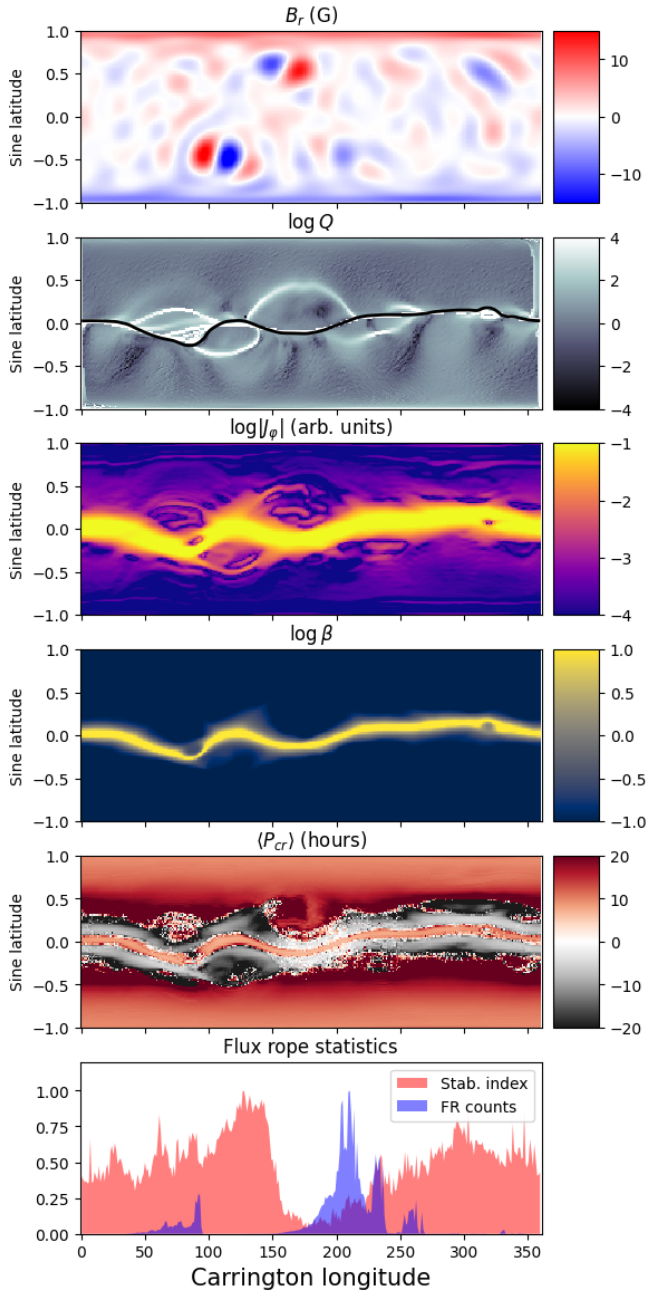

Fig. 10. Spatial structure of the June 14 simulation. *Top panel* shows the surface magnetic field obtained from the ADAPT magnetogram. The *second panel* displays the logarithm of the squashing factor Q. The maximum of Q matches the HCS, shown in black, while secondary arches indicates QSLs. The *third panel* shows the logarithm of the azimuthal current J_φ at $3\,R_\odot$. Maxima are located at the HCS with some variation of intensity along the sheet. Currents also appear at quasi-separatrices. The *fourth panel* shows the logarithm of the β parameter at $3\,R_\odot$. Higher β are observed at the HCS and close to the HCS/QSLs intersections. The average $\langle P_{\rm cr}(r = 3\,R_\odot)\rangle$ is shown in the *fifth panel*, displaying consistently stable regions at the QSL/HCS intersections. Finally, the *last panel* shows the normalized histogram of detected flux ropes in the simulation in blue and the stability index described in the text.

In Fig. 10, we analyze the 3D longitudinal distribution of these flux ropes. In the top panel, we show the structure of the surface magnetic field imposed as the boundary condition in the simulation of June 14. We observe notably two strong bipolar structures, around 100° and 150° longitude, that correspond to two active regions present at the time. The 3D structure of the MHD solution is obviously largely shaped by the structure of the surface magnetic field. However, features in the solar wind, that is, beyond closed regions extending to a few $R_\odot$ are more easily interpreted computing the network of separatrices and quasi-separatrices. In the second panel of Fig. 10, we plot the squashing factor Q in logarithmic scale as a longitude versus latitude synoptic map. The value of Q is computed between two spherical surfaces at $r = r_\odot$ and $r = 5\,R_\odot$ following the formulation given in Titov (2007). The HCS, defined as $B_r(\theta, \varphi) = 0$, is shown in black and corresponds to the maximum of the current. The squashing factor identifies high gradients and discontinuities in the connectivity of field lines, and thus either true separatrices like the HCS where Q should be in principle infinite, or QSLs for high values ($Q \geq 10^3$). The QSLs form arched structures that correspond in general to the location of pseudo-streamer fans. The two bipoles around 100° longitude create pseudo-streamers and the largest structures in the network of QSLs. Their signatures can be seen in most other MHD variables.

In the second panel, we show a cut of the logarithm of $|J_\varphi|$ at $r = 3\,R_\odot$. Although most of the current structures are located around the HCS, weaker currents are present along the QSLs. Magnetic field shears can indeed be easily created there following small perturbations (see Aulanier et al. 2005, 2006). The structure of quasi-separatrices is also visible in β, plotted in the fourth panel of Fig. 10. At the HCS/QSLs intersections, we observe significant β values (as well as slower wind speeds). This higher β regime corresponds both to increased densities and lower magnetic field amplitude (in particular B_r). These extended large β values also correspond to slightly weaker currents, as the HCS is thicker is these regions. In the fifth panel, we show the time averaged $\langle P_{\rm cr}\rangle$ at $3\,R_\odot$ between $t = 60$ h and $t = 180$ h. As in Fig. 9, the gray-black colors indicate stable zones where magnetic tension contains the pressure gradient. Here again a structure is shaped by the network of quasi-separatrices. At most HCS/QSLs intersections, we observe very dark patches, which mark consistently stable zones over the period. Finally, the bottom panel displays the normalized histogram of every flux rope detected between $t = 60$ h and $t = 180$ h and $r = 5\,R_\odot$ and $10\,R_\odot$ in the simulation of June 14. The detection algorithm is as follows: we trace magnetic field lines from seed points in a regular grid close to the HCS and between 5 and $10\,R_\odot$, and we identify a flux rope when the number of sign changes of B_r is larger than four along a given field line. This procedure can count multiple field lines that belong to the same flux rope at a given time and may also catch the same propagating structure from one simulation output to the other (which are spaced by two hours). Hence, we normalize the distribution by its maximum to get a value between 0 and 1. This provides a general distribution of flux ropes occurrence in the simulation. As already noted in Fig. 8, some longitudes are marked by more flux ropes than others and we report the highest concentration of flux ropes between the longitudes of 150° and 270°.

These longitudes correspond to regions where the surrounding of the HCS, the heliospheric plasma sheet, is only marginally stable, shown as the white-clear regions in the fifth panel of Fig. 10. In contrast, we notice a very clear stable zone between 100° and 150° in longitude, where no flux rope are detected in the simulations. More precisely, we observe in the simulation lower temperatures and lower pressure gradients $\nabla p/p$ within QSLs. Typically, at $3\,R_\odot$, the plasma is around 1MK along the QSLs, while it is around 2MK in other open field regions. As the pressure gradients are lower, the regions around HCS/QSLs intersections are more stable. To carry out a quantitative test of

this results, we computed (in addition to the normalized statistics of flux ropes) a stability index, which is the sum on all latitudes of negative values of $\langle P_{\rm cr} \rangle$ normalized to fall back in the interval $[0, 1]$. This index is shown in red in the last panel of Fig. 10. We then computed the Pearson correlation coefficient between the stability index and the flux ropes' count. We obtained a coefficient of -0.42, which indicates a statistically significant anti-correlation – no correlation is 0, while a perfect (anti-)correlation is $(-)1$. We reproduce this analysis in Fig. A.1 for the simulation of June 1 and we find similar results.

5. Summary and discussion

In this work, we combined multi-spacecraft, multi-instrument analyses with 3D MHD simulations to investigate the origin of the helical structures in the slow solar wind. We took advantage of the conjunction of the Parker Solar Probe fifth perihelion in June 2020 with the first measurements of Solar Orbiter and ran 3D MHD simulations of the inner heliosphere at this period, from the chromosphere to 0.5 AU. In contrast with a previous study carried out at the first perihelion of PSP in November 2018, during a period of relatively low solar activity (Réville et al. 2020a), several active regions have appeared during the month of June 2020. These rising phases of solar activity are associated with the formation of small coronal holes appearing at low latitudes in the active region belt (Wang et al. 2010). As such, synoptic magnetic maps are shown to have evolved significantly over the whole month, and we found that one single simulation could not accurately reproduce the state of the inner heliosphere over the period, especially around the HCS. We looked for the optimal number and instances of synoptic magnetic field maps among the ADAPT database, and found that two maps, and thus two simulations, could reasonably render the magnetic sectors measured by Parker Solar Probe and Solar Orbiter.

Reproducing the right magnetic sectors correctly is indeed necessary (but not sufficient) to identify and numerically model the sources of the solar wind. Comparing the in situ plasma data of PSP and Solar Orbiter with the simulations, we have shown a good overall agreement of the magnetic field amplitude, proton density, and radial velocity. In the synthetic measurements drawn from the simulations, we can observe periods of high and low variability in the density and velocity fields. These tend to occur when the probe is either crossing or close to the simulated HCS. Because both PSP and Solar Orbiter are confined to relatively low latitudes, they are bound to frequently cross the HCS and cruise in the heliospheric plasma sheet, and although there are many additional sources of variability in the actual data (Alfvén waves, switchbacks), we do find a good correspondence between regions of strong variability in the simulations, and region of low cross-helicity and high plasma beta, namely, when the spacecraft is close to the HCS. We further analyzed the data from PSP to identify individual HCS crossings and flux rope events, using, in particular, the pitch-angle distributions of suprathermal electrons (see Figs. 6 and 5).

Our simulations also reproduce flux ropes confined to the HCS, which are created at the tip of helmet streamers by a succession of instabilities. First, a pressure driven instability extends and thins the current sheet. Then a tearing mode disrupts the sheet, triggering reconnection following a guide field in the super-alfvénic regime. This process is very similar to the one described in 2.5D by Réville et al. (2020b), in which we clearly identified the characteristics of the resistive tearing mode as the source of chains of plasmoids released in the slow wind. However, as shown in Réville et al. (2020b), the complete tearing process cannot be fully characterized in a low Lundquist numbers regime. In this work, we ran ideal MHD simulations and the resistivity was set by the numerical grid and scheme. We estimated the Lundquist number to be around $500-1000$, close to the reconnection region of the simulations. The threshold to trigger the tearing mode is thus lower in these 3D simulations than in the 2.5D configuration studied in Réville et al. (2020b). This result is consistent with several recent 3D numerical works (see, e.g., Oishi et al. 2015; Yang et al. 2020), for which the tearing instability is observed for Lundquist number of a few thousand. Moreover, the work of Lotfi & Hosseinpour (2021) has shown that the presence of an inhomogeneous guide field could lead to an enhanced growth rate of the tearing instability. More generally, the complex configurations induced by the realistic magnetic fields must change the picture in comparison with the purely axisymmetric case; however, since coronal Lundquist numbers should be substantially greater than in our simulations and on the order of $S \sim 10^{14}$, we would expect tearing instabilities to occur naturally during the HCS formation process.

The simulations confirm the ability of sequential magnetic reconnection at the tip of helmet streamers to produce flux ropes in the HCS (see also Higginson & Lynch 2018, for another 3D study). These flux ropes are first connected on both sides to the Sun, but can also reconnect later in the open solar wind, which is consistent with typical observed electrons pitch-angle distributions. The 3D simulations also reveal a long periodicity of the flux rope release, about 20 h, corresponding to the formation and re-formation of the HCS after the pressure driven instability. Following Peterson et al. (2021), we computed the characteristic timescale of this process and we recover the long timescale (20 h–30 h) observed in 2.5D and 3D simulations. We note that in Peterson et al. (2021), the heuristics yields shorter frequencies, directly identified to the main peak of observed periodic density perturbations of the solar wind, which are around 90 min (Viall & Vourlidas 2015). However, their computation does not include the gravity pull, which leads to an interesting difference between the latter and the present work. Removing the gravitational acceleration in Eq. (5), we find an average periodicity of the order of 3 h. However, we also find that without gravity, the whole inner corona is unstable to pressure gradient forces, which means that gravity does play an important role in the force balance in these regions. Hence, while these authors claim that the specific details of the tearing mode do not matter to reach agreement with observations, we argue that the fastest growing mode of the ideal tearing is necessary to go down to the hour-long timescales, as shown in Réville et al. (2020b).

Finally, we observed a well-defined structure in the longitudinal distribution of flux rope events. The global MHD solution is shaped by the topology of the magnetic field and, in particular, the structure of separatrices and quasi-separatrices, which can be easily identified with the squashing factor Q. We obtained the following results: slower wind, higher beta, lower temperatures, and lower currents at most intersections of the QSLs with the HCS. These intersections are consequently less prone to the pressure driven instability and they determine the end of the reconnection line – and, thus, the extent of the flux rope. It is not trivial to generalize this result to high S regimes, as we can expect the current sheets to always be unstable to the tearing mode for a low enough finite resistivity (Biskamp 1986). Nonetheless, the pressure instability analysis is expected to be robust in any resistive regime. Further studies are necessary to characterize the structure of flux ropes in 3D realistic configurations and higher S regimes. This is crucial for a better understanding of the connectivity in the HCS, which can be shown to

be completely different from what has been predicted by static models.

Acknowledgements. This research was funded by the ERC SLOW_SOURCE project (SLOW_SOURCE – DLV-819189). V. R., M. V., C. S. acknowledge discussions within the HERMES DRIVE Science center team. The authors are grateful to A. Mignone and the PLUTO development team. Simulations were performed on the Jean-Zay supercomputer (IDRIS), through GENCI HPC allocations grants A0090410293 and A0110410293. Parker Solar Probe was designed, built, and is now operated by the Johns Hopkins Applied Physics Laboratory as part of NASA's Living with a Star (LWS) program. The SWEAP and FIELDS investigations are supported by the PSP mission under NASA contract NNN06AA01C. Solar Orbiter is a space mission of international collaboration between ESA and NASA, operated by ESA. Solar Orbiter Solar Wind Analyser (SWA) data are derived from scientific sensors which have been designed and created, and are operated under funding provided in numerous contracts from the UK Space Agency (UKSA), the UK Science and Technology Facilities Council (STFC), the Agenzia Spaziale Italiana (ASI), the Centre National d'Études Spatiales (CNES, France), the Centre National de la Recherche Scientifique (CNRS, France), the Czech contribution to the ESA PRODEX programme and NASA. Solar Orbiter SWA work at UCL/MSSL is currently funded under STFC grants ST/T001356/1 and ST/S000240/1. Solar Orbiter magnetometer operations are funded by the UK Space Agency (grant ST/T001062/1). This work utilizes data produced collaboratively between AFRL/ADAPT and NSO/NISP. Data analysis was performed with the help of the AMDA science analysis system provided by the Centre de Données de la Physique des Plasmas (CDPP) supported by CNRS, CNES, Observatoire de Paris and Université Paul Sabatier, Toulouse. Work at IRAP and LAB was performed with the support of CNRS and CNES. A.S.B. and A.S. were supported by a CNES Solar Orbiter grant and PNST. S.P. acknowledges the funding by CNES through the MEDOC data and operations center. This study has made use of the NASA Astrophysics Data System.

References

Altschuler, M. D., & Newkirk, G. 1969, Sol. Phys., 9, 131
Antiochos, S. K., Mikić, Z., Titov, V. S., Lionello, R., & Linker, J. A. 2011, ApJ, 731, 112
Antiochos, S. K., Linker, J. A., Lionello, R., et al. 2012, Space Sci. Rev., 172, 169
Arge, C. N., Henney, C. J., Koller, J., et al. 2010, in Twelfth International Solar Wind Conference, eds. M. Maksimovic, K. Issautier, N. Meyer-Vernet, M. Moncuquet, & F. Pantellini, AIP Conf. Ser., 1216, 343
Arge, C. N., Henney, C. J., Hernandez, I. G., et al. 2013, in Solar Wind 13, eds. G. P. Zank, J. Borovsky, R. Bruno, et al., AIP Conf. Ser., 1539, 11
Aulanier, G., Pariat, E., & Démoulin, P. 2005, A&A, 444, 961
Aulanier, G., Pariat, E., Démoulin, P., & DeVore, C. R. 2006, Sol. Phys., 238, 347
Badman, S. T., Bale, S. D., Martínez Oliveros, J. C., et al. 2020, ApJS, 246, 23
Bale, S. D., Goetz, K., Harvey, P. R., et al. 2016, Space Sci. Rev., 204, 49
Biskamp, D. 1986, Phys. Fluids, 29, 1520
D'Amicis, R., Perrone, D., Bruno, R., & Velli, M. 2021, J. Geophys. Res. (Space Phys.), 126, e28996
Dedner, A., Kemm, F., Kröner, D., et al. 2002, J. Comput. Phys., 175, 645
DeForest, C. E., Howard, R. A., Velli, M., Viall, N., & Vourlidas, A. 2018, ApJ, 862, 18
Démoulin, P., Priest, E. R., & Lonie, D. P. 1996, J. Geophys. Res., 101, 7631
Einaudi, G., Boncinelli, P., Dahlburg, R. B., & Karpen, J. T. 1999, J. Geophys. Res., 104, 521
Endeve, E., Leer, E., & Holzer, T. E. 2003, ApJ, 589, 1040
Endeve, E., Holzer, T. E., & Leer, E. 2004, ApJ, 603, 307
Furth, H. P., Killeen, J., & Rosenbluth, M. N. 1963, Phys. Fluids, 6, 459
Gosling, J. T., Skoug, R. M., McComas, D. J., & Smith, C. W. 2005, Geophys. Res. Lett., 32, L05105
Higginson, A. K., & Lynch, B. J. 2018, ApJ, 859, 6
Higginson, A. K., Antiochos, S. K., DeVore, C. R., Wyper, P. F., & Zurbuchen, T. H. 2017, ApJ, 840, L10
Horbury, T. S., OBrien, H., Carrasco Blazquez, I., et al. 2020, A&A, 642, A9
Kasper, J. C., Abiad, R., Austin, G., et al. 2016, Space Sci. Rev., 204, 131
Laker, R., Horbury, T. S., Bale, S. D., et al. 2021, A&A, 652, A105
Lavraud, B., Fargette, N., Réville, V., et al. 2020, ApJ, 894, L19
Lionello, R., Linker, J. A., & Mikić, Z. 2009, ApJ, 690, 902
Lotfi, H., & Hosseinpour, M. 2021, Front. Astron. Space Sci., 8, 176
Loureiro, N. F., Schekochihin, A. A., & Cowley, S. C. 2007, Phys. Plasmas, 14, 100703
Mignone, A., Bodo, G., Massaglia, S., et al. 2007, ApJS, 170, 228
Müller, D., Marsden, R. G., St. Cyr, O. C. , & Gilbert, H. R. 2013, Sol. Phys., 285, 25
Müller, D., St. Cyr, O. C., Zouganelis, I., et al. 2020, A&A, 642, A1
Oishi, J. S., Mac Low, M.-M., Collins, D. C., & Tamura, M. 2015, ApJ, 806, L12
Owen, C. J., Bruno, R., Livi, S., et al. 2020, A&A, 642, A16
Peterson, E. E., Endrizzi, D. A., Clark, M., et al. 2021, J. Plasma Phys., 87, 905870410
Priest, E. R., & Démoulin, P. 1995, J. Geophys. Res., 100, 23443
Pucci, F., & Velli, M. 2014, ApJ, 780, L19
Rappazzo, A. F., Velli, M., Einaudi, G., & Dahlburg, R. B. 2005, ApJ, 633, 474
Réville, V., Velli, M., Rouillard, A. P., et al. 2020a, ApJ, 895, L20
Réville, V., Velli, M., Panasenco, O., et al. 2020b, ApJS, 246, 24
Rouillard, A. P., Davies, J. A., Forsyth, R. J., et al. 2008, Geophys. Res. Lett., 35, L10110
Rouillard, A. P., Davies, J. A., Lavraud, B., et al. 2010, J. Geophys. Res. (Space Phys.), 115, A04103
Sanchez-Diaz, E., Rouillard, A. P., Davies, J. A., et al. 2017, ApJ, 835, L7
Sanchez-Diaz, E., Rouillard, A. P., Lavraud, B., Kilpua, E., & Davies, J. A. 2019, ApJ, 882, 51
Schatten, K. H., Wilcox, J. M., & Ness, N. F. 1969, Sol. Phys., 6, 442
Sheeley, N. R., Wang, Y. M., Hawley, S. H., et al. 1997, ApJ, 484, 472
Stansby, D., Rai, Y., Argall, M., et al. 2021, heliopython/heliopy: HelioPy 0.15.4
Tenerani, A., Velli, M., Rappazzo, A. F., & Pucci, F. 2015, ApJ, 813, L32
Titov, V. S. 2007, ApJ, 660, 863
Titov, V. S., & Démoulin, P. 1999, A&A, 351, 707
Titov, V. S., Hornig, G., & Démoulin, P. 2002, J. Geophys. Res. (Space Phys.), 107, 1164
Tu, C.-Y., & Marsch, E. 1995, Space Sci. Rev., 73, 1
Velli, M., Harra, L. K., Vourlidas, A., et al. 2020, A&A, 642, A4
Viall, N. M., & Vourlidas, A. 2015, ApJ, 807, 176
Viall, N. M., Kepko, L., & Spence, H. E. 2009, J. Geophys. Res. (Space Phys.), 114, A01201
Viall, N. M., Spence, H. E., Vourlidas, A., & Howard, R. 2010, Sol. Phys., 267, 175
Wang, Y. M., Sheeley, N. R. J., & Walters, J. H. 1998, ApJ, 498, L165
Wang, Y. M., Robbrecht, E., Rouillard, A. P., Sheeley, N. R. J., & Thernisien, A. F. R. 2010, ApJ, 715, 39
Yang, L., Li, H., Guo, F., et al. 2020, ApJ, 901, L22

Appendix A: June 1 simulation

Figure A.1, repeats the same analysis as done for Figure 10 for the simulation of June 1. At this time, the lower hemisphere active region (AR) has not appeared on the solar disk (it will on June 3 at around 100° of longitude). The AR around 320 degrees appears stronger compared to the June 14 map. The current sheet shows a significantly weaker warp and a simpler QSLs and current structures. However, at high longitudes, we do observe a complex structure of QSLs and a thickening of the HCS. Stable regions with few flux ropes are thus located at longitudes between 250 and 330 degrees of longitudes. The Pearson correlation coefficient between the flux ropes counts and the normalized stability curve is −0.3.

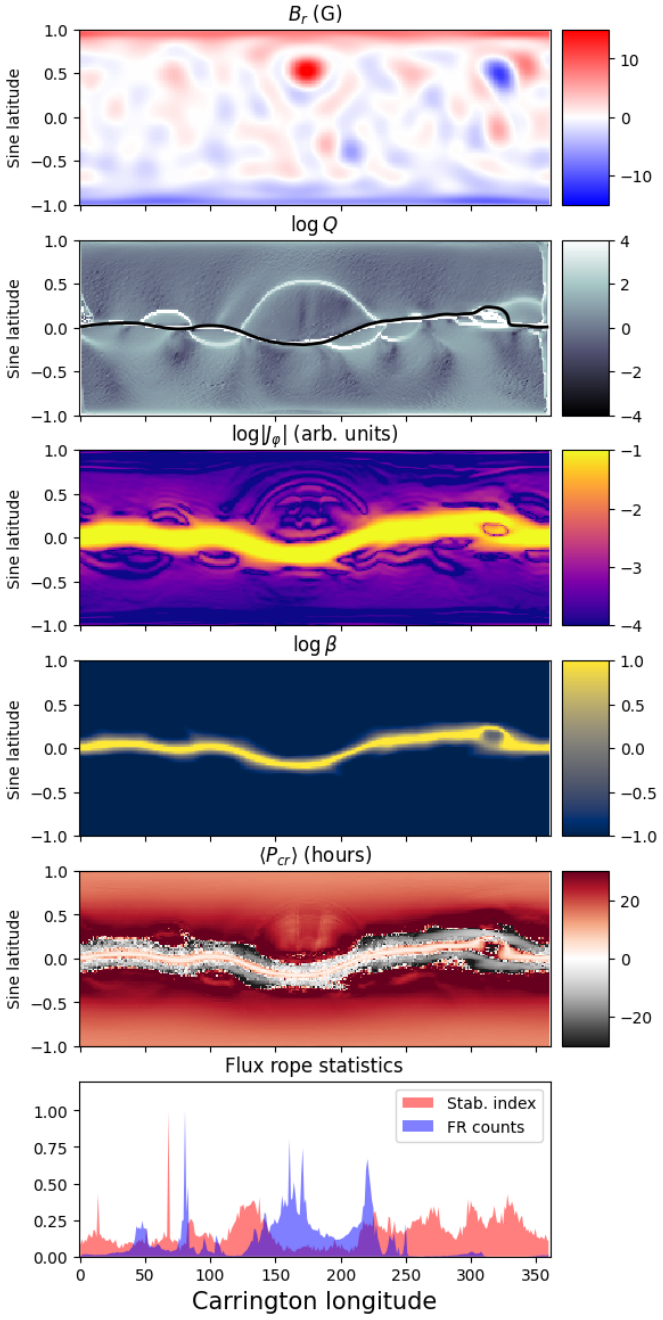

Fig. A.1. Spatial structure of the June 1 simulation. Top panel shows the surface magnetic field obtained from the ADAPT magnetogram. The second panel displays the logarithm of the squashing factor Q. The HCS is shown in black, while secondary arches indicates QSLs. The third panel shows the logarithm of the azimuthal current J_φ at $3R_\odot$. Maxima are located at the HCS with some variation of intensity along the sheet. Currents also appear at quasi-separatrices. The fourth panel shows the logarithm of the β parameter at $3R_\odot$. Higher β are observed at the HCS and close to the HCS/QSLs intersections. The average $\langle P_{cr}(r = 3R_\odot)\rangle$ is shown in the fifth panel, displaying consistently stable regions at the QSL/HCS intersections. Finally, the last panel shows the normalized histogram of detected flux ropes in the simulation in blue and the stability index described in the text.

Appendix B: Flux rope and HCS crossings identification

Table B.1. Identified (partial) Heliospheric Current Sheet (PHCS/HCS) crossings, Coronal Mass Ejections (CMEs), and Flux Ropes (FR) in PSP data during the month going from May 28, 2020, to June 29, 2020

#	Start	End	Description
1	2020-05-27 17h00	2020-05-28 04h00	HCS with FRs
2	2020-05-28 08h58	2020-05-28 14h55	CME
3	2020-05-29 21h40	2020-05-30 04h31	CMEs
4	2020-05-31 00h00	2020-05-31 07h00	HCS with FRs
5	2020-05-31 13h04	2020-05-31 03h19	PHCS with CMEs/FR
6	2020-06-01 10h20	2020-06-01 12h16	PHCS
7	2020-06-01 12h52	2020-06-01 13h02	HCSs
8	2020-06-01 14h36	2020-06-01 16h10	CME
9	2020-06-01 19h21	2020-06-01 21h36	HCSs and FR
10	2020-06-02 06h41	2020-06-02 09h19	CMEs with HCS
11	2020-06-04 03h30	2020-06-04 06h05	PHCS
12	2020-06-07 07h07	2020-06-07 08h50	CME
13	2020-06-07 11h19	2020-06-07 12h34	PHCS
14	2020-06-07 20h16	2020-06-07 21h09	PHCS with FRs
15	2020-06-07 23h30	2020-06-08 12h30	HCS with FRs
16	2020-06-08 15h30	2020-06-09 01h40	HCS with FRs
17	2020-06-12 01h30	2020-06-12 07h50	CME
18	2020-06-16 16h00	2020-06-17 14h00	PHCS with FRs
19	2020-06-18 08h00	2020-06-18 12h30	HCSs with FRs
20	2020-06-18 18h40	2020-06-19 00h30	HCSs with FRs
21	2020-06-19 11h10	2020-06-20 12h00	HCSs with FRs
22	2020-06-21 06h00	2020-06-21 14h00	HCSs with FRs
23	2020-06-23 07h00	2020-06-23 17h00	HCSs with FRs
24	2020-06-24 12h00	2020-06-25 03h00	HCSs with FRs
25	2020-06-25 11h00	2020-06-27 12h00	CME (Fig. B.1)

In this work, we visually inspected PSP data from May 28, 2020 to June 29, 2020, in order to identify structures linked to HCS dynamics such as heliospheric current sheet crossings (HCSs), flux ropes (FRs) and coronal mass ejections (CMEs). Although our intention has been to be as objective as possible, this selection does rely on a visual inspection. For reproducibility purposes, we provide the list of the identified structures in table B.1. The HCS crossings were identified by a reversal of the radial component of the magnetic field associated with a change in the pitch-angle distribution (PAD) of the suprathermal electron population (strahl) that is consistent with its outward propagation. We identify flux ropes based on their classical signatures, namely, an increase in the magnetic pressure and a bipolar signature in one of the components of the magnetic field. The boundaries of the events were defined based on variations in the profiles of the magnetic and plasma parameters.

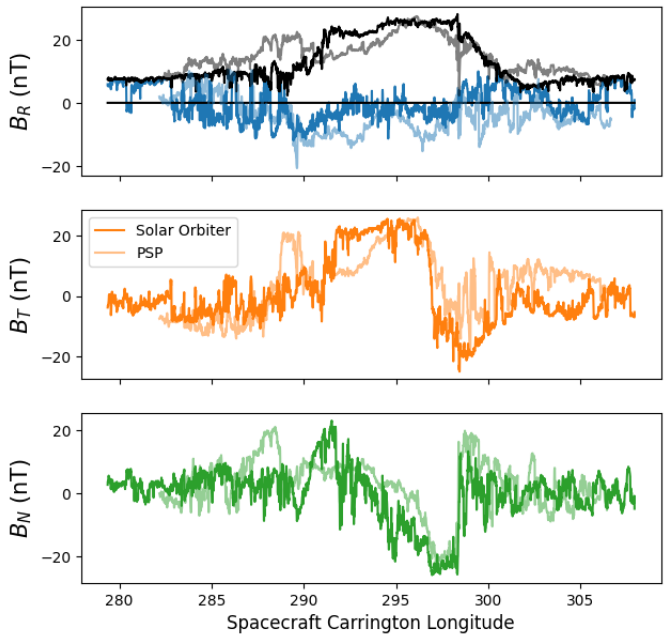

Fig. B.1. Two CME event discovered in the vicinity of the HCS by Solar Orbiter and PSP one month apart. The Carrington longitude of PSP is shifted by 17 degrees to superpose the structures. The total field $\|B\|$ is shown in black (Solar Orbiter)/gray (Parker Solar Probe) in the top panel.

In Figure 6, we overlay in red all the HCS, PHCS, and FR events of this table. Because the relationship between CMEs and the HCSs is beyond the scope of this paper, we have removed all pure CME events of Figure 6. However, we were intrigued to discover a very similar CME event observed one month apart by both PSP and Solar Orbiter. The CME is reported as the 25th event of Table B.1, measured between June 25 and June 27. Solar Orbiter measured another CME between May 28 and May 30. In Figure B.1, we show the magnetic field structure of the two events as a function of the Carrington longitude of each spacecraft. We added 17 degrees to the longitude of PSP to superpose the structures. The amplitude, orientation, and overall structures of the two CMEs are very close, which suggests that they might share a similar origin.